Rare Metal Materials and Engineering
Volume 54, Issue 7, July 2025
Available online at www.rmme.ac.cn

Science Press

Cite this article as: Gao Huixian, Shao Shan, Li Qinqin, et al. Effect of Hot Deformation on α-Phase Precipitation and Mechanical Properties of Metastable β Titanium Alloy[J]. Rare Metal Materials and Engineering, 2025, 54(07): 1706-1716. DOI: https://doi.org/10.12442/j.issn.1002-185X.20240316.

ARTICLE

Effect of Hot Deformation on α-Phase Precipitation and Mechanical Properties of Metastable β Titanium Alloy

Gao Huixian[1,2], Shao Shan[2], Li Qinqin[2], Li Yuze[3], Wang Xiyu[2], Lei Qiang[2], Wang Tao[2], Luo Wenzhong[1,2], Liu Xianghong[1,2], Feng Yong[1,2]

[1] School of Materials Science and Engineering, Northwestern Polytechnical University, Xi'an 710072, China; [2] Western Superconducting Technologies Co., Ltd, Xi'an 710018, China; [3] School of Physical Science and Technology, Northwestern Polytechnical University, Xi'an 710072, China

Abstract: The effect of hot deformation on α-phase precipitation during the subsequent heat treatment, as well as the mechanical properties of TB18 Ti-alloy, was investigated. Results show that the round bar obtained by the dual-phase field forging of the cast ingot exhibits uniform composition distribution on its cross-section. However, various degrees of deformation are detected at different positions on the cross-section, which is attributed to the characteristics of the forging process. Under the forging condition, the microstructure is mainly composed of β-phase matrix and coarsened discontinuous primary α-phases. After solution and following artificial aging treatment, the primary α-phases disappear, while needle-like secondary α-phases precipitate in the matrix. Additionally, dispersed white zones are observed in the samples after aging, which are analyzed to be the precipitation-free zones of secondary α-phase. Despite a uniform compositional distribution among various regions, these dispersed white zones exhibit higher content and larger size in the positions that have undergone lower forging deformation. It indicates that the insufficient forging deformation inhibits the precipitation of the secondary α-phase, ultimately resulting in the lower strengthening effect by heat treatment. Thus, consistent with the characteristics of the forging process, a periodic variation of sample in strength is detected along the circumferential direction of the forged round bar.

Key words: metastable β Ti-alloy; hot deformation; heat treatment; α-phase precipitation; mechanical property

1 Introduction

Titanium alloys have been widely employed in aerospace, aviation, marine and other industries for many years owing to their attractive comprehensive properties like high specific strength, superior toughness, excellent corrosion resistance and superior compatibility[1–3]. Compared to near-α Ti-alloys and α+β Ti-alloys, metastable β Ti-alloys exhibit superior cold formability and enable the optimization of both high strength and high toughness, owing to the variety of complex microstructures achievable through aging treatments[4–7]. Therefore, metastable β alloys have emerged as the preferred material for fabricating ultra-high-strength and high-toughness titanium alloys, gradually supplanting α+β titanium alloys as the primary material for large-scale aviation backbone forgings[8–10].

During the hot deformation of the metastable β Ti-alloys, as well as the following heat treatment, the α-phase precipitates in the β-phase matrix. The morphology, volume fraction, size and distribution of α-phase precipitation in the alloy vary depending on the cooling rate and other heat treatment parameters[11–15]. For example, Wang et al[12] found that the volume fraction of α-phase decreased under solution heat treatment, accompanied with the decrease in tensile strength. The size and volume fraction of α-phase increased during the aging heat treatment after solution, accompanied by an increase in both strength and fracture toughness. With the increase in size and decrease in amount of the α-phase, the

Received date: July 28, 2024
Foundation item: Qin Chuangyuan Cites High-Level Innovation, Entrepreneurship Talent Project (QCYRCXM-2023-003); Innovation Capability Support Program of Shaanxi (2022KJXX-84)
Corresponding author: Liu Xianghong, Ph. D., Professor, Western Superconducting Materials Technologies Co., Ltd, Xi'an 710018, P. R. China, E-mail: xhliu@c-wst.com

strengthening effect of α-phases decreased. The volume fraction of primary α-phase in Ti-1023 alloy plays the primary role in influencing the mechanical properties.

The $\beta \rightarrow \alpha$ phase transformation and the precipitation behavior of the α-phase are also impacted by the deformation process[16–22]. Wan et al[16] found that cold pre-deformation markedly influences the aging behavior and mechanical properties of Ti-1300 alloys. The microstructures of the pre-deformation samples, which were aged at 550 °C, contain α-phases in β matrix regardless of cold deformation reduction after solution treatment. Fine/uniform and coarse/needle-like α precipitates are formed in the slightly and heavily deformed zones, respectively. Hua et al[17] found that the α -phase globularization and the improved kinetics of the $\beta \rightarrow \alpha$ phase transformation occurred due to the thermo-mechanical processing under the hot compression of Ti-5553 alloy. The significant influence of deformation on the phase transformation could be attributed to the formation of nucleation sites by microstructural defects such as deformation bands and dislocations. Song et al[19] found that a variant of parallel α plates was generally observed in the prestrained and aged Ti-10Mo-8V-1Fe-3.5Al alloy samples. During the aging process, the α platelets randomly nucleated in β matrix in the unstrained samples, while in the prestrained samples, the α-phases precipitated along slip bands and grain boundaries where dislocation density was high, resulting in web-like structures at early aging stage. Morita et al[21] reported that the cold rolling after the solution treatment accelerated the aging kinetics in Ti-20V-4Al-1Sn alloy. Especially when the sample subjected to 70% rolling reduction, the α-phase precipitation occurred in only 6 s at 773 K.

The provided information suggests that in near-β titanium alloys, the transformation of the β-phase into a needle-like α-phase constitutes the primary mechanism for alloy strengthening. The preceding deformation behaviour plays a crucial role in the subsequent $\beta \rightarrow \alpha$ transformation during heat treatment. However, most of the research has focused on the formation of the α-phase during the deformation process. Moreover, the precise mechanisms governing the influence of deformation on α-phase precipitation and its correlation with mechanical properties remain elusive. The purpose of this study is to investigate the effect of hot deformation during the forging process on the $\beta \rightarrow \alpha$ transformation and the mechanical properties of a novel near-β titanium alloy TB18 (Ti-4Al-5Mo-5V-5Cr-1Nb).

2 Experiment

TB18 (Ti-4Al-5Mo-5V-5Cr-1Nb, wt%) alloy was fabricated by a vacuum consumable arc melting furnace. The β transus temperature (T_β) of this TB18 alloy is 800±5 °C. The ingots were remelted three times to ensure compositional homogeneity and the elimination of impurities. Subsequently, the forging-processed bars with a diameter of 400 mm were obtained through several times of duplex forging at β region and $\alpha+\beta$ region. The parameters of the forging process are shown in Fig.1.

Fig.2 shows the schematic diagram of the forging process. In the forging process, a cylindrical ingot underwent initial shaping into a quadrilateral form, as depicted in Fig. 2a, in which four distinct planes labeled A, B, C and D (referred to as the large surfaces) were produced, as illustrated in Fig. 2b. The following forging produced a cylindrical bar with a diameter of Φ400 mm as the final state. For experimental purposes, two pieces with the specified thickness were cut from the forged bar to serve as samples.

Considering the inherent characteristics of forging, it is known that the large surfaces exhibit minimal deformation due to the restricted fluidity of the metal during forging. In contrast, significant deformation is expected at the corners. Consequently, four samples were selected from both the large

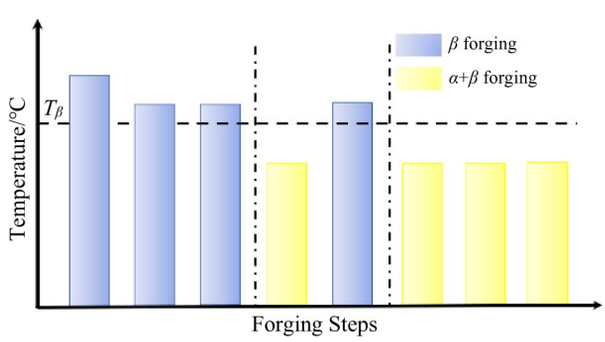

Fig.1 Schematic diagram of forging process and parameters

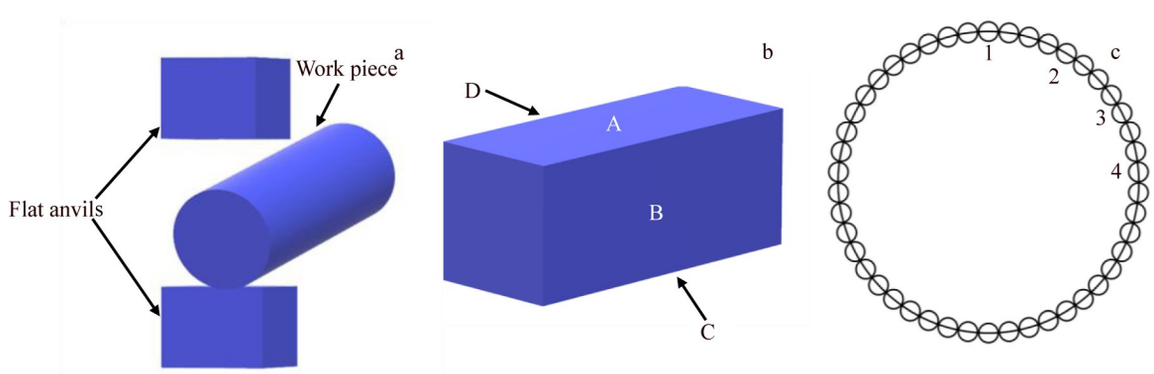

Fig.2 Schematic diagram of forging process (a), quadrilateral shape of rod after first forging (b), and selected positions for analysis (c)

surfaces and the corners, denoted by positions 1, 2, 3 and 4, as shown in Fig.2c. The four-position sampling strategy aimed to cover approximately a quarter of the entire specimen, thereby representing the overall performance of the specimen blank.

The four positions of the two pieces were divided into two groups: one group referred to forging state (R state), while the other underwent the following heat treatment (HT state). The HT state samples were solution treated at 870 °C for 1 h and subsequently air cooled (AC), followed by the aging process at 525 °C for 4 h. Details pertaining to the heat treatment system and sample information are presented in Table 1.

In summary, this experimental design systematically investigates the impact of forging and heat treatment on samples extracted from different positions within a forged bar. The focus is on assessing variations in deformation and performance, with specific attention to differences between the large surface and edge corner positions.

Samples taken from all positions under each state were prepared for microstructural examinations. These samples were ground to 2000# abrasive paper, mechanically polished, and then etched in the solution of HF: HNO_3: H_2O=5: 20: 75. The microstructures and composition were examined and analyzed by optical microscope (OM, Olympus GX71) and scanning electron microscope (SEM, JSM-IT700HR). Electron backscatter diffraction (EBSD) observations were conducted on JSM-IT700HR to characterize the microstructural features. The samples used for EBSD observation were prepared by ion sputtering polishing method. The samples for tensile tests were cut into tensile samples with the gauge length of 25 mm and a diameter of 5 mm, as presented in Fig. 3. Then, they were stretched on a Zwick Universal Testing Machine (Zwick 330 KN) at a strain rate of 0.2 s^{-1} at room temperature.

3 Results

3.1 Phase component and microstructure of forged sample

The metallographic microstructures of the four samples under the forged state are shown in Fig.4a–4d. All samples are primarily composed of continuous β-phase matrix in gray and discontinuous blocky α -phase in black. In the high-magnification microstructure of the same samples presented in Fig.4e–4h, the α-phase is observed to be spherical or short rod-shaped, with no significant differences among the four samples. It is evident that the R2C sample exhibits a smaller quantity of α-phase compared to the other three samples.

According to the metallographic microstructures of the forged samples in Fig. 4, R1F and R2C, which were cut from two typical position of the forged rod, show the most significant differences. Thus, these two samples were selected for the following analyses as the representatives.

Fig. 5 presents energy-dispersive X-ray spectroscope (EDS) element mappings of R1F and R2C samples. The elemental contents from the EDS result for each sample are summarized in Table 2. The result reveals that the elemental distribution maintains a uniform state in the samples after forging, with no noticeable element segregation. Furthermore, there are no discernible differences in elemental distribution at different positions of the forged billet.

To determine the phase composition of samples from different positions, X-ray diffraction (XRD) tests were conducted on samples from all four positions, and the results are presented in Fig. 6. The diffraction peaks in Fig. 6 indicate that the phase composition of samples in the R state from different positions is primarily composed of α -Ti, β -Ti, NbTi39 and MoNb. Among these phases, α -Ti and β -Ti constitute the majority of the composition. Consequently, in the subsequent EBSD characterization process, two distinct analytical phases, α-Ti and β-Ti, were established. The results of EBSD characterization demonstrate a uniform distribution of components in both samples. For the R1F sample, the α-Ti content is 14.8%, and the β-Ti content is 82.5%. In the R2C sample, the α-Ti content is 15.7%, and the β-Ti content is 81.1%. According to XRD analysis and EBSD characterization results, it is evident that in the R state, the α-Ti content in R2C sample is higher than that in R1F sample.

Table 1 Details pertaining to heat treatment system and sample information

Designation	State	Position	Heat treatment parameter
R1F, R4F	Forged	Large surfaces 1, 4	/
R2C, R3C	Forged	Corners 2, 3	/
HT1F, HT4F	Heat treated	Large surfaces 1, 4	870 °C/1 h, AC, 525 °C/4 h
HT2C, HT3C	Heat treated	Corners 2, 3	870 °C/1 h, AC, 525 °C/4 h

Due to the restrictions of OM and SEM in providing clear grain information of the forged samples, EBSD was employed for crystallographic orientation mapping, grain boundary characterization and inverse pole figures (IPFs), as depicted in Fig. 7. From Fig. 7, it is evident that both samples consist of large and small grains, with the R2C sample exhibiting smaller average grain size and a higher proportion of smaller

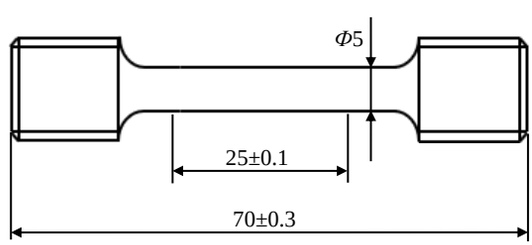

Fig.3 Schematic diagram of tensile sample

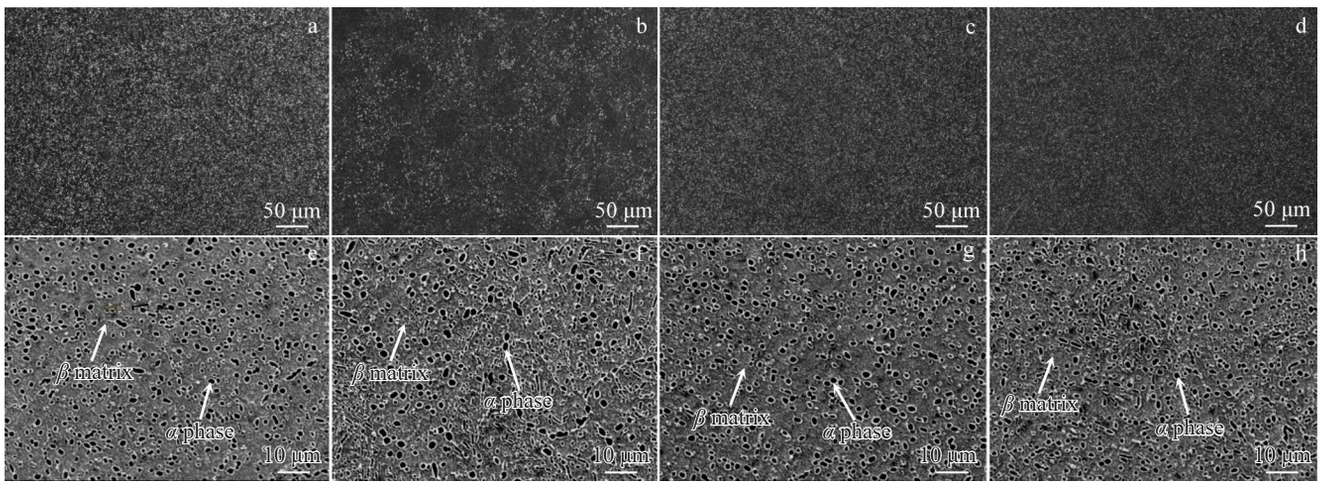

Fig.4 Metallographic microstructures of forged samples: (a, e) R1F, (b, f) R2C, (c, g) R3C, and (d, h) R4F

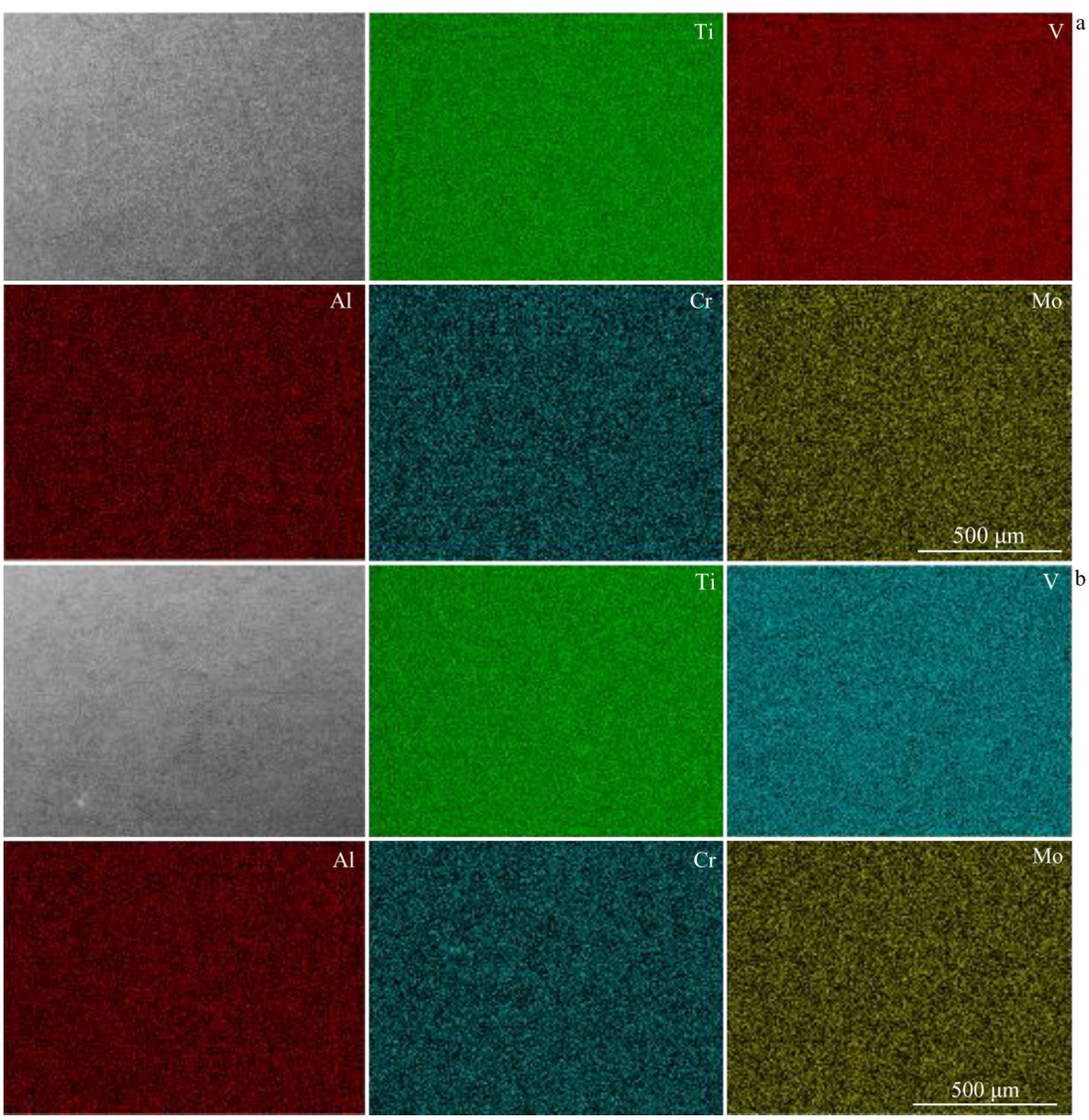

Fig.5 EDS element mappings of forged samples: (a) R1F; (b) R2C

grains. In the R1F sample, the proportion of small-angle grain boundaries is 59.2%, while large-angle grain boundaries account for 40.8%. In contrast, the R2C sample has a higher proportion of small-angle grain boundaries (63.7%) and a

Table 2 Elemental contents of forged samples in Fig.5 (wt%)

Sample	Ti	Mo	V	Cr	Al	Nb
R1F	71.56	5.10	4.96	5.17	3.42	0.93
R2C	71.16	4.95	4.74	4.84	3.79	0.90

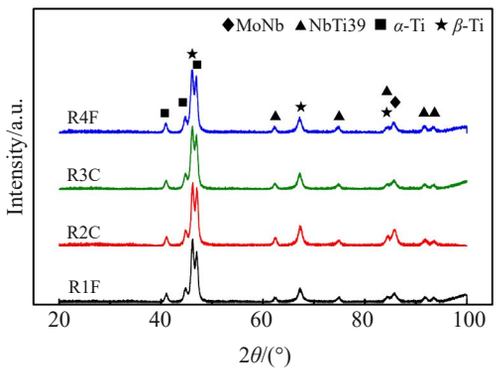

Fig.6 XRD patterns of forged samples

lower proportion of large-angle grain boundaries (36.3%). The R2C sample displays a higher percentage of small-angle grain boundaries. Analyzing the IPF maps of both samples for the β-Ti phase, it is observed that in the z-direction, a majority of grains exhibit a {001} texture, indicating that the axial direction of the rod-shaped sample is perpendicular to the {001} crystal planes of these grains. The other two directions show less pronounced textures. In comparison, the R2C sample exhibits a more distinct texture in IPF maps than the R1F sample.

Fig. 8 and Table 3 depict the kernel average misorientation (KAM) values and area proportion obtained through EBSD analysis for the two samples. KAM values are the measurement results of local misorientation angles within the sample. They serve to characterize the geometric dislocation density within the sample, reflecting the degree of plastic deformation. Higher KAM values indicate a greater degree of plastic deformation or higher defect density[23]. Upon statistical analysis of KAM values and their distribution for both samples, it is evident that the R2C sample exhibits a higher average KAM value. Additionally, the proportion of regions with high KAM values is larger in the R2C sample. This observation indicates that the R2C sample underwent more significant deformation and experienced a higher degree

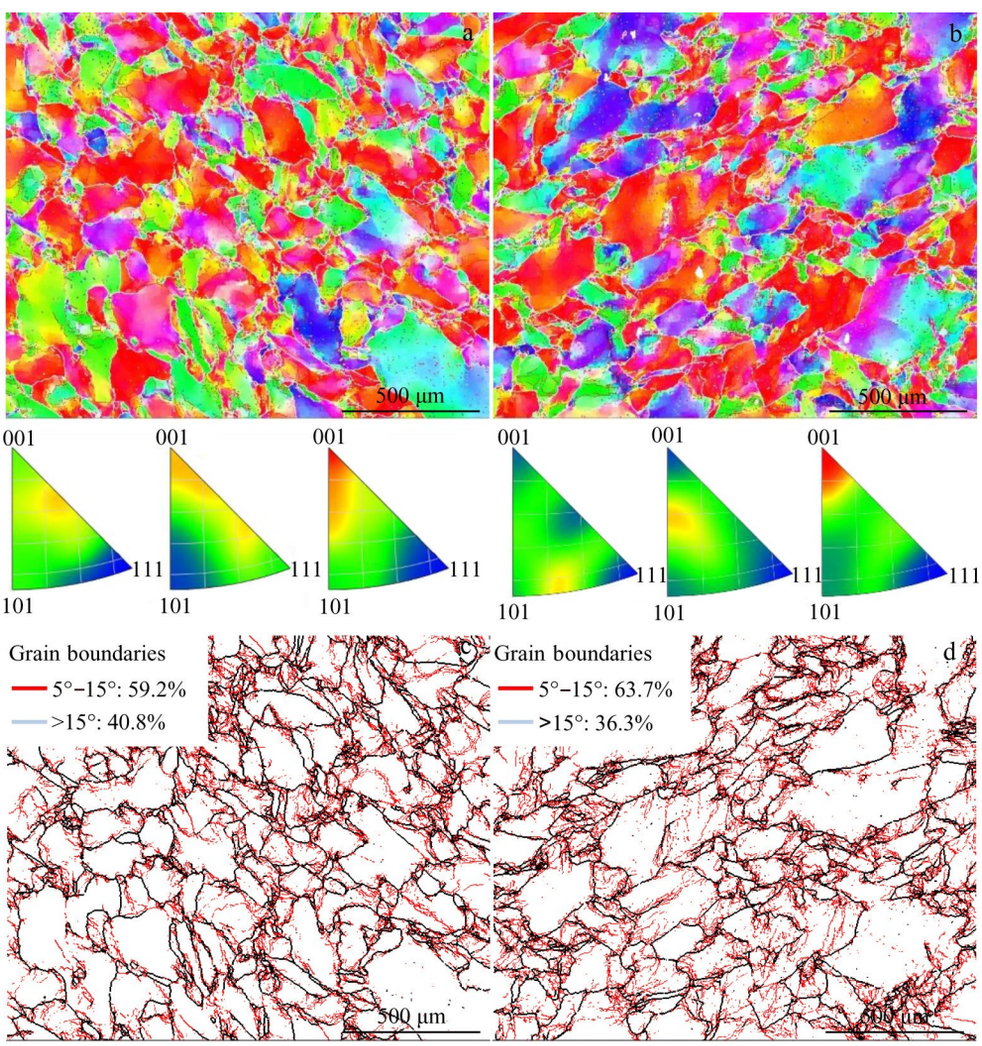

Fig.7 EBSD maps with IPFs (a–b) and distribution of grain boundaries (c–d) of forged samples: (a, c) R1F; (b, d) R2C

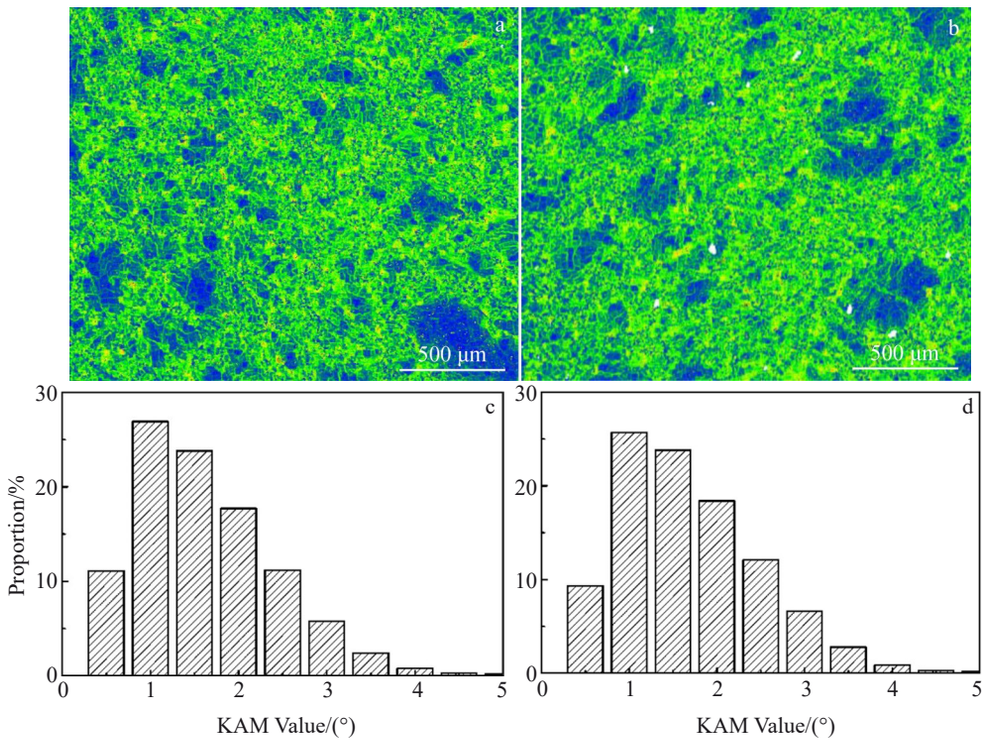

Fig.8 KAM mappings (a–b) and distribution of KAM values (c–d) of forged samples: (a, c) R1F; (b, d) R2C

Table 3 Area proportion of KAM values for forged samples (%)

Sample	0°–1.2°	1.2°–2.5°	2.5°–3.7°	3.7°–5.0°
R1F	50.6	40.1	8.7	0.8
R2C	47.5	41.8	10.0	0.8

of plastic deformation during the forging process compared to the R1F sample.

3.2 Phase component and microstructure of heat treated sample

The microstructures of the two selected samples under the heat treated state are shown in Fig. 9. The metallographic microstructures reveal significant differences between HT1F and HT2C samples. In the HT1F sample, a substantial amount of white region is observed, as illustrated in the magnified view of the white rectangle in Fig.9a. The white dashed circle delineates the white region within that area, as shown in Fig.9b. In the HT2C sample, as shown in Fig.9d–9e, there is a much less presence of white regions. For both samples, the distribution of the white regions is relatively uniform.

SEM observation was conducted on the white regions and other regions except the white regions inside the grain, as shown in Fig. 9c and 9f for HT1F and HT2C, respectively. From these figures, it is evident that the β matrix, containing supersaturated stabilizing elements, is transformed from a body-centered cubic structure (β-phase) to a densely packed hexagonal structure (α-phase) in most region of the samples after solution heat treatment and aging. The resulting α-phase exhibits a needle-like morphology, as pointed by the black arrow in Fig. 9f. In the HT2C sample, the secondary α-phase precipitates in a finer and more uniformly distributed manner near grain boundaries and within the grains. However, no α-phase is detected in the white regions, referring to the precipitates-free region, as pointed out by the white arrows in Fig.9c and 9f.

Fig.10 presents EDS element mappings of HT1F and HT2C samples. The elemental content from EDS for each sample is summarized in Table 4. Combining the information from Fig. 10 and Table 4, it is evident that the elements in both samples maintain a uniform state after forging and heat treatment, with no noticeable element segregation. Furthermore, there are no discernible differences in elemental distribution at different positions, even between the white regions and other regions of the grain.

XRD results of the heat treated samples, as illustrated in Fig. 11, show that apart from a significant reduction in the α-phase content in the HT2C sample, there is minimal change in the other major phases compared to the R state. Consistent with EBSD characterization in the R state, two analytical phases, α-Ti and β-Ti, were defined during EBSD characterization process. The analytical results from the characterization of the two samples reveal that the HT1F sample has the α-Ti content of 4.6% and the β-Ti content of 94.6%, while the HT2C sample has the α-Ti content of 0.3% and the β-Ti content of 99.4%. The higher α-Ti content in HT1F indicates a more substantial presence of the α-phase, whereas HT2C sample exhibits nearly negligible α-phase, suggesting that during the heat treatment process, the original α-phase has completely dissolved into the matrix and reprecipitated in the form of needle-like structures.

From EBSD maps of the heat treated samples shown in Fig.12, it can be observed that the grain sizes are uniform and

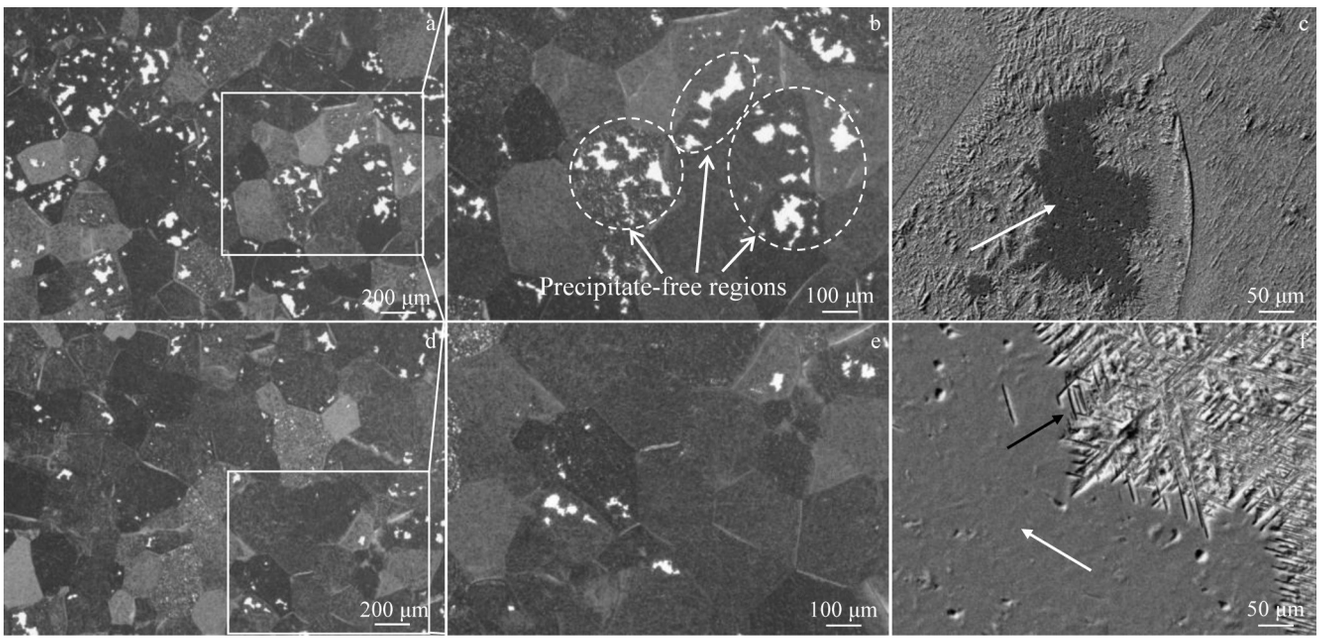

Fig.9 Metallographic microstructures (a–b, d–e) and SEM images (c, f) of heat treated samples: (a–c) HT1F; (d–f) HT2C

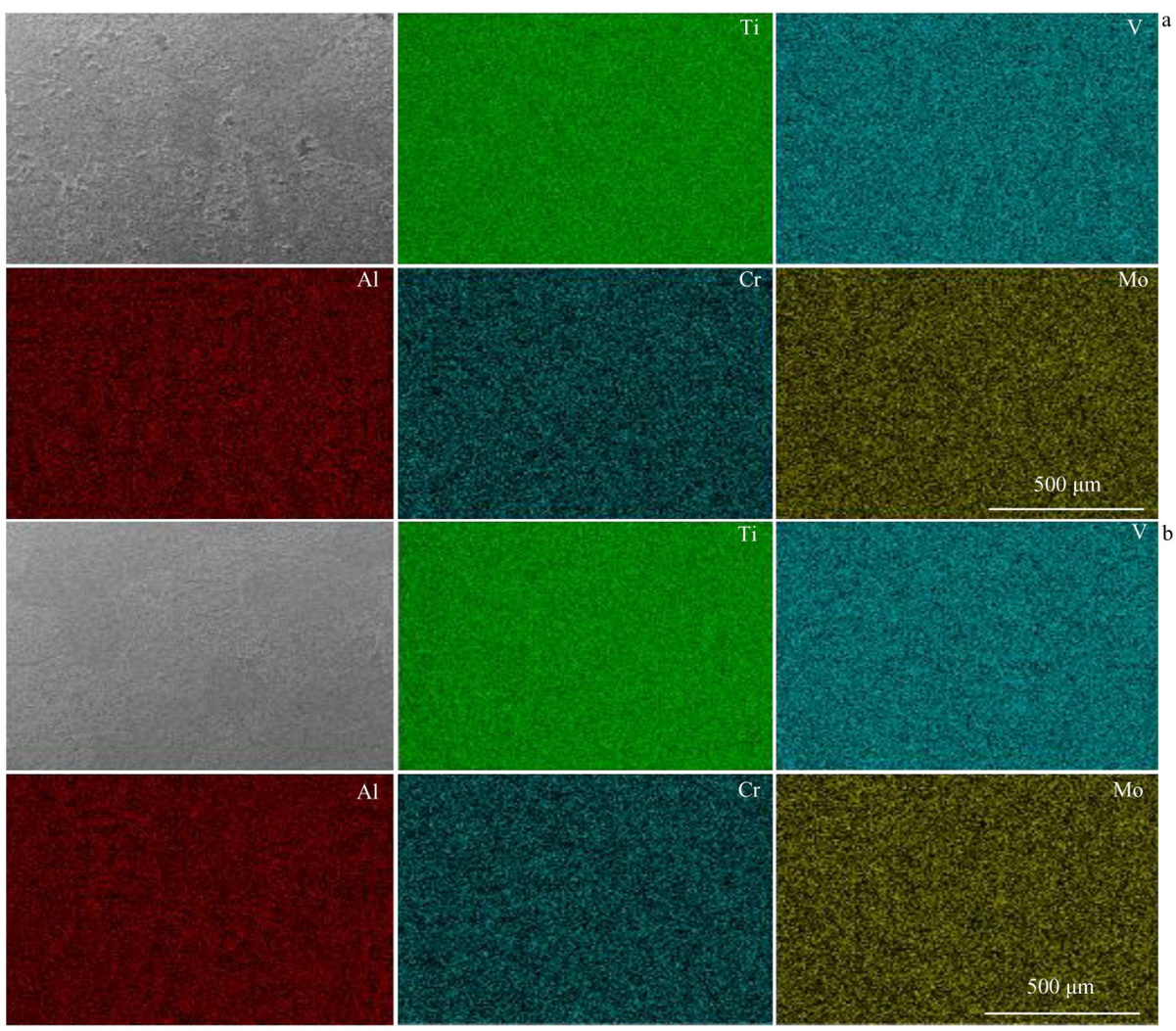

Fig.10 EDS element mappings of heat treated samples: (a) HT1F; (b) HT2C

Table 4 Elemental contents for heat treated samples in Fig. 10 (wt%)

Sample	Ti	Mo	V	Cr	Al	Nb
HT1F	71.16	4.95	4.74	4.87	3.79	0.90
HT2C	70.64	4.63	4.74	4.89	3.82	0.94

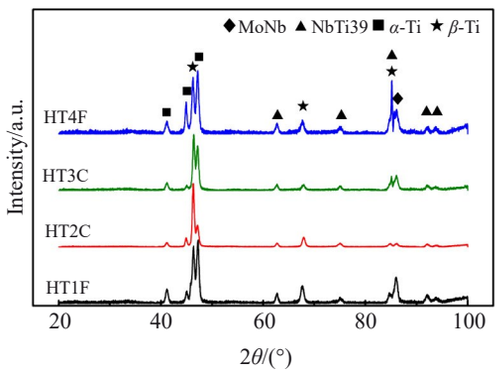

Fig.11 XRD patterns of heat treated samples

the grains exhibit significant recrystallization after heat treatment. In the HT1F sample, a portion of subgrains is still present, while in the HT2C sample, the grain sizes are more uniform. Disregarding the presence of subgrains, the average grain size in HT2C is finer, indicating a more pronounced recrystallization. In the HT1F sample, small-angle grain boundaries account for 5.55%, while large-angle grain boundaries account for 94.5%. In the HT2C sample, small-angle grain boundaries account for 4.96%, and large-angle grain boundaries account for 95.0%. The proportion of small-angle grain boundaries is lower in HT2C, further indicating more recrystallization. No significant texture for the β-phase is observed in both samples.

3.3 Analysis of mechanical properties

The tensile test results of the 46 samples from all positions of the circular piece cut from the forged rod under heat treated condition, and the four selected samples (positions 1, 2, 3, 4 mentioned in section 2) under both forged and heat treated conditions are presented in Fig. 13b and 13c, respectively. The data from the 46 tests are color-coded and plotted in Fig. 13a, where red represents samples with higher strength, yellow represents samples with lower strength and orange represents samples with strength between the higher and lower strength ranges. Three samples with dashed lines experienced tensile fracture outside the gauge length, rendering their experimental results invalid. The tensile strength profile in Fig. 13b exhibits a noticeable fluctuating trend with peaks and valleys at the positions indicated by yellow and red markers in Fig. 13a, respectively. Upon investigating the positions corresponding to these points, it is observed that samples with higher strength, located at peak values, are positioned at the edges formed after forging, while samples with lower strength, located at valley values, are positioned on the large forged surface.

From Fig. 13a, it is apparent that the strength of samples at different positions transitions from high strength at the edges to low strength at the large surface. Extracting the values of two peaks and two valleys and plotting them in Fig. 13c provide a more intuitive view of the strength changes after

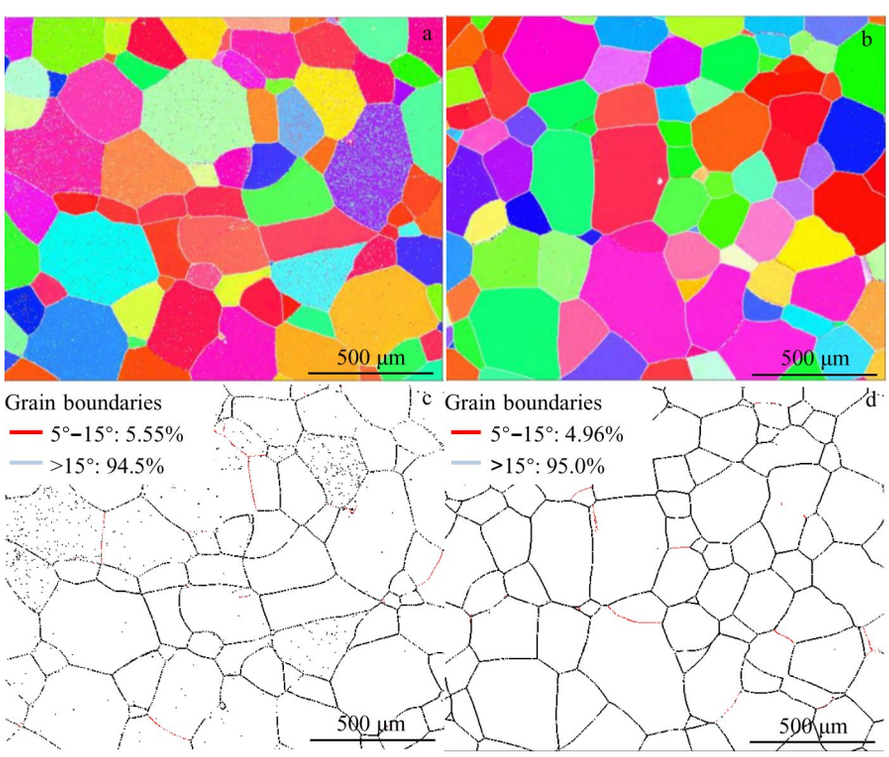

Fig.12 EBSD maps (a–b) and distribution of grain boundaries (c–d) of forged samples: (a, c) HT1F; (b, d) HT2C

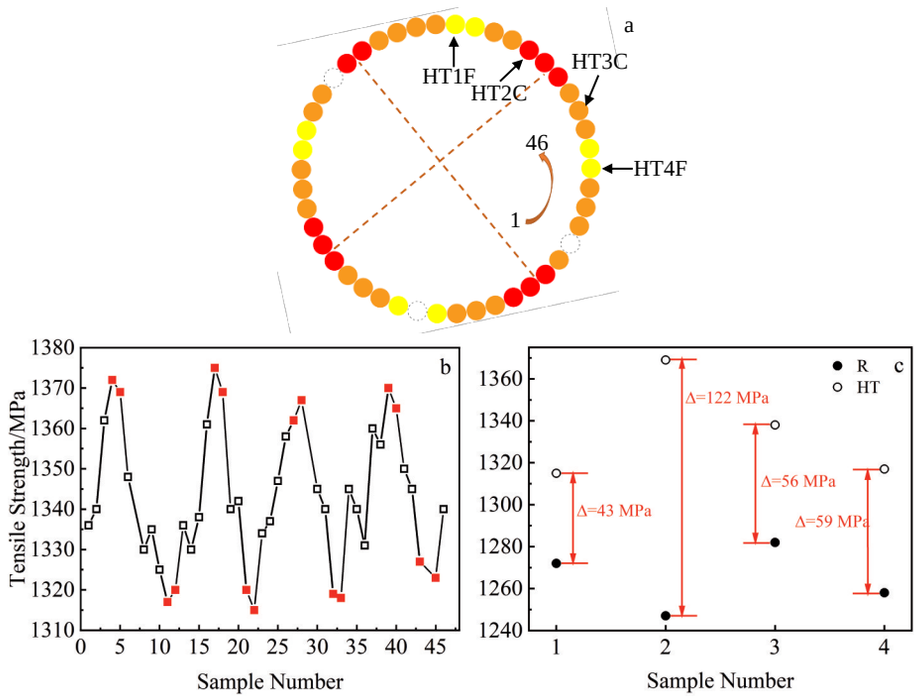

Fig.13 Schematic diagram of 46 samples from different positions of circular piece (a); tensile test results of 46 samples under HT state (b) and selected positions 1, 2, 3, and 4 under both R state and HT state (c)

heat treatment. In Fig. 13c, black hollow symbols represent samples in R state, while black solid symbols represent samples in HT state. Table 5 presents the mechanical performance results for samples in both states after tensile testing, indicating higher mechanical performance in HT state. Among HT samples, sample number 2 and 3 at the edges exhibit higher strength, while sample number 1 and 4 at the large surface exhibit lower strength.

4 Discussion

4.1 Relationship of microstructure and position on forged billet

In the forged state, as shown in Fig. 4, the R2C samples exhibit a higher content of soft primary α-phase, resulting in lower strength in the forged condition. During the forging process, the material flow in the large surface area is restricted, leading to reduced deformation. In contrast, at the edges formed by forging extrusion, the material flow is increased, resulting in higher deformation. In this region, a significant number of fine dispersed plate-like α-phases precipitate in the β matrix after heat treatment. These α-phases, appearing as fine needles, effectively impede dislocation movement, thereby enhancing the strength.

4.2 Effect of deformation on precipitation and its mechanism

The precipitation characteristics of the α-phase depend on the deformation heat treatment process of materials. Particularly during hot compression simulation, the nucleation position, morphology, size and orientation relationships of the α-phase are more complex compared to conditions involving sole heat treatment. Thermal deformation significantly influences the precipitation characteristics of the α-phase, and the morphology and precipitation locations of the α-phase may change due to the presence of external stress. Under the combined action of heat and force, the α-phase and β-phase may no longer follow the Burgers orientation relationship.

A large number of crystallographic defects (dislocations, subgrain boundaries, slip bands, etc.) generated during alloy hot deformation provide preferential nucleation sites for the precipitation of the α-phase, promoting its precipitation[24–25]. The alloy undergoes continuous dynamic recovery and recrystallization during the thermal deformation process, and it is influenced by the dual effects of kinetics and thermodynamics[26]. With increasing deformation or temperature, the distortion energy increases, leading to the redissolution of primary α-phases into the β matrix. As the temperature decreases and the distortion energy decreases, the body-centered cubic structure of the β matrix is transformed into the densely packed cubic structure of the α-phase.

When the alloy undergoes a certain amount of deformation, crystal defects are introduced, which assist the nucleation of the α-phase. With the increase in deformation, a larger

Table 5 Tensile strength of samples in R state and HT state (MPa)

Sample	R1F	R2C	R3C	R4F	HT1F	HT2C	HT3C	HT4F
Tensile strength	1272	1247	1282	1258	1315	1369	1338	1317

number of defects in the alloy reduce the nucleation barrier required for heterogeneous nucleation, resulting in the formation of the dense continuous α-phase in regions with high dislocation density, as well as in areas with small-grain thickness and at grain boundaries.

From the analysis of EBSD results in this experiment and the knowledge of the position of R2C sample at the forged edges, it is evident that R2C sample undergoes significant deformation. Therefore, during the aging process, the precipitation of secondary α-phases provides more energy, promoting the precipitation of the secondary α-phases. Additionally, in EBSD observations of the amples in HT state, it is found that the grain size of the HT2C sample is smaller than that of the HT1F sample. During the aging process, oversaturated α-stabilizing elements undergo continuous $\beta \rightarrow \alpha$ phase transformation with atomic diffusion. Larger grain sizes inevitably increase the diffusion distance, causing the α-phase to precipitate continuously along strip-like patterns, ultimately increasing its final length. Simultaneously, due to factors such as diffusion distance, larger areas of the unprecipitated region appear.

4.3 Relationship between microstructure and mechanical properties under HT condition

The primary α-phases formed in the R state often exhibit a coarse spherical (or elongated rod-shaped) morphology, coexisting with the β matrix, resulting in poor overall performance. After solution treatment, a single β-phase is formed with the appropriate cooling rate. This not only eliminates the uneven structure caused by dynamic processes during hot working, but also effectively controls the content of primary α-phases.

Following solution treatment, the β matrix undergoes further aging, during which the α-stabilizing elements in the β-phase are gradually segregated, leading to the phase transformation and the precipitation of fine dispersed strengthening α-phases. This significantly enhances the strength of the alloy. In the process of plastic deformation, the precipitation phases in β-Ti alloys strengthen the material. Its principle is that the hindrance of secondary α-phases to dislocation movement increases the strength of the alloy.

The relationship between the volume fraction of secondary α-phases, their geometric dimensions and the mechanical properties can be expressed by Eq. (1)[27]:

$$\sigma = f\left(\frac{f_{\alpha_s}}{d_{\alpha_s}}\right) \quad (1)$$

where σ is the yield strength, f is the volume fraction, d is the size of the precipitated phase, and α_s is the secondary α-phase. It is evident that as the volume fraction of secondary α-phases increases, their size decreases, and the yield strength of the alloy increases. In Fig. 10, post-heat-treatment analysis of samples HT1F and HT2C reveals that sample HT2C exhibits higher strength owing to a more uniform and finer distribution of secondary α-phases.

5 Conclusions

1) After dual-phase field forging, the ingot of the forged Ti-4Al-5Mo-5V-5Cr-1Nb alloy obtains a round bar with uniform composition distribution on the cross-section. The microstructure is primarily composed of β-phase matrix and rod-like or spherical α-phase. The forging process induces varying degrees of deformation at different positions on the cross-section.

2) After solution and aging treatment, the microstructure is primarily composed of β-phase matrix and needle-like secondary α-phase. Additionally, all samples exhibit dispersed precipitate-free regions of α-phases, although there is no difference in composition among various regions.

3) In regions with lower degree of forging deformation, the content and size of precipitate-free regions after heat treatment are larger, suggesting that increasing forging deformation enhances the precipitation of the needle-like secondary α-phases.

4) Samples with lower forging deformation exhibit lower strength after heat treatment. Along the circumferential direction of the forged round bar, the strength distribution demonstrates periodic fluctuations.

References

1 Boyer R R. *Materials Science and Engineering A*[J], 1996, 213(1–2): 103

2 Banerjee D, Williams J C. *Acta Materialia*[J], 2013, 61(3): 844

3 Cui C X, Hu B M, Zhao L C *et al. Materials & Design*[J], 2011, 32(3): 1684

4 Peters M, Hemptenmacher J, Kumpfert J *et al. Titanium and Titanium Alloys*[M]. Chicheste: John Wiley & Son Inc, 2003: 1

5 Fan J K, Li J S, Zhang Y D *et al. Advanced Engineering Materials*[J], 2017, 19(7): 1600859

6 Rodrigues M, Carla M. *Phase Transformation Studies in a Metastable Beta Ti-5553 Alloy and Near Alpha Ti-Mo Alloys*[D]. Vancouver: University of British Columbia, 2022

7 Zhao Q Y, Chen Y N, Xu Y K *et al. Materials & Design*[J], 2021, 200: 109457

8 Cotton J D, Briggs R D, Boyer R R *et al. JOM*[J], 2015, 67(6): 1281

9 Zhang F, Feng J, Xiang W *et al. Materials Science and Engineering A*[J], 2022, 858: 144082

10 Wang Q, Ren J Q, Xin C *et al. Materials Science and Engineering A*[J], 2023, 867: 144753

11 Lütjering G, Williams J C. *Titanium*[M]. Berlin: Springer, 2007: 283

12 Wang Xiaoyan, Liu Jianrong, Lei Jiafeng *et al. Acta Metallurgica Sinica*[J], 2007, 43(11): 1129 (in Chinese)

13 Kumar S, Kamath R, NandwanA P *et al. Materialia*[J], 2020, 14: 100883

14 Ghasemi E, Zarei-hanzaki A, Moemeni S *et al. Materials Science and Engineering: A*[J], 2016, 654: 264

15 Mutombo K, Siyasiya C, Stumpf W E. *International Conference on Advanced Materials Research*[C]. Zurich: Trans Tech Publications Ltd, 2014: 584
16 Wan M P, Zhao Y Q, Zeng W D *et al. Journal of Alloys and Compounds*[J], 2015, 619: 383
17 Hua K, Xue X Y, Kou H C *et al. Journal of Alloys and Compounds*[J], 2014, 615: 531
18 Meng L, Kitashima T, Tsuchiyama T *et al. Metallurgical and Materials Transactions A*[J], 2020, 51(11): 5912
19 Song Z Y, Sun Q Y, Xiao L *et al. Materials Science and Engineering A*[J], 2010, 527(3): 691
20 Nandal V, Sarvesha R, Singh S S *et al. Journal of Alloys and Compounds*[J], 2021, 855: 157521
21 Morita T, Murakami k. *Materials Transactions*[J], 2012, 53(1): 173
22 Chandiran E, Nagata Y, Sun F *et al. Metallurgical and Materials Transactions A*[J], 2021, 52(7): 3107
23 Kamaya M, Wilkinson A J, Titchmarsh J M. *Acta Materialia*[J], 2006, 54(2): 539
24 Du Jingwen, An Bailing, Zhang Lin *et al. Rare Metal Materials and Engineering*[J], 2023, 52(1): 403 (in Chinese)
25 Zhang Changjiang, Ji Xiang, Sun Yonggang *et al. Rare Metal Materials and Engineering*[J], 2022, 51(4): 1531 (in Chinese)
26 Cherukuri B, Srinivasan R, Tamirisakandala S *et al. Scripta Materialia*[J], 2009, 60(7): 496
27 Jaffee R I. *Progress in Metal Physics*[J], 1958, 7: 65

热变形对亚稳态β钛合金α相析出及力学性能的影响

高慧贤[1,2]，邵　珊[2]，李芹芹[2]，李玉泽[3]，王玺玉[2]，雷　强[2]，王　涛[2]，罗文忠[1,2]，刘向宏[1,2]，冯　勇[1,2]
(1. 西北工业大学 材料学院，陕西 西安 710072)
(2. 西部超导材料科技股份有限公司，陕西 西安 710018)
(3. 西北工业大学 物理科学与技术学院，陕西 西安 710072)

摘　要：研究了热变形对TB18钛合金后续热处理过程中α相析出以及力学性能的影响。结果表明：通过双相区锻造工艺获得的圆棒，在其横截面上表现出均匀的成分分布。然而由于锻造工艺的特点，在横截面不同位置的变形程度不同。在锻造状态下，显微组织主要由β相基体和粗大不连续的初生α相组成。经过固溶处理和人工时效后，粗大初生α相消失，针状次生α相在基体中弥散析出。此外，时效后的样品中观察到分散的白色区域，经分析为次生α相未析出区域。尽管锻造后各个区域的成分分布均匀，但在锻造变形较小的位置，白色区域的含量更高，尺寸明显更大。这表明锻造变形不足抑制二次α相的析出，最终导致热处理强化效果降低。因此，与锻造工艺过程特征一致，样品沿着锻造圆棒的圆周方向，强度呈现周期性变化。

关键词：亚稳态β钛合金；热变形；热处理；α相析出；力学性能

作者简介：高慧贤，女，1981年生，硕士，高级工程师，西部超导材料科技股份有限公司，陕西 西安 710018，E-mail：gaohuixian@c-wst.com